

Hydrated Manganese(II) Phosphate ($\text{Mn}_3(\text{PO}_4)_2 \cdot 3\text{H}_2\text{O}$) as a Water Oxidation Catalyst

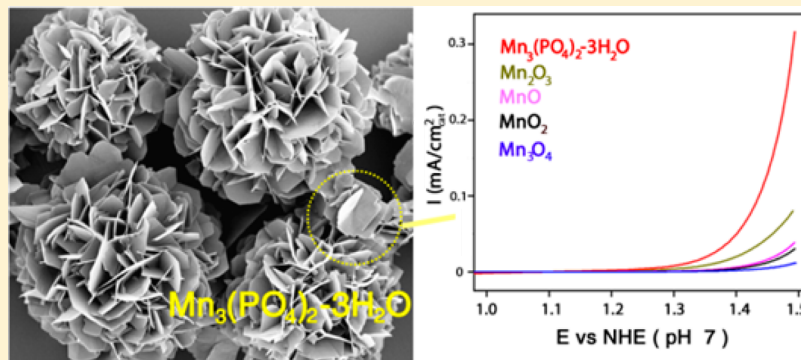
Kyoungsuk Jin,^{†,‡,§} Jimin Park,^{†,‡,§} Joohee Lee,^{†,‡} Ki Dong Yang,^{†,‡} Gajendra Kumar Pradhan,^{†,‡} Uk Sim,^{†,‡} Donghyuk Jeong,^{†,‡} Hae Lin Jang,^{†,‡} Sangbaek Park,^{†,‡} Donghun Kim,[§] Nark-Eon Sung,^{||} Sun Hee Kim,[§] Seungwu Han,^{†,‡} and Ki Tae Nam*,^{†,‡}

[†]Department of Materials Science and Engineering and [‡]Research Institute of Advanced Materials (RIAM), Seoul National University, Seoul 151-744, Korea

[§]Division of Materials Science, Korea Basic Science Institute, Daejeon 305-333, Korea

^{||}Pohang Accelerator Laboratory, POSTECH, Pohang 790-784, South Korea

S Supporting Information



ABSTRACT: The development of a water oxidation catalyst has been a demanding challenge in realizing water splitting systems. The asymmetric geometry and flexible ligation of the biological Mn_4CaO_5 cluster are important properties for the function of photosystem II, and these properties can be applied to the design of new inorganic water oxidation catalysts. We identified a new crystal structure, $\text{Mn}_3(\text{PO}_4)_2 \cdot 3\text{H}_2\text{O}$, that precipitates spontaneously in aqueous solution at room temperature and demonstrated its high catalytic performance under neutral conditions. The bulky phosphate polyhedron induces a less-ordered Mn geometry in $\text{Mn}_3(\text{PO}_4)_2 \cdot 3\text{H}_2\text{O}$. Computational analysis indicated that the structural flexibility in $\text{Mn}_3(\text{PO}_4)_2 \cdot 3\text{H}_2\text{O}$ could stabilize the Jahn–Teller-distorted Mn(III) and thus facilitate Mn(II) oxidation. This study provides valuable insights into the interplay between atomic structure and catalytic activity.

INTRODUCTION

Splitting water into hydrogen and oxygen is a promising pathway for solar energy conversion and storage systems.^{1–7} The oxygen evolution reaction (OER) has been regarded as a major bottleneck in the overall water splitting process due to the slow transfer rate of the four electrons involved and the high activation energy barrier for O–O bond formation.^{8–14} In nature, there is a water oxidation complex (WOC) in photosystem II (PSII) composed of the earth-abundant elements, Mn and Ca.^{7,13–16} The WOC in PSII, in the form of a cubical CaMn_4O_5 cluster, efficiently catalyzes water oxidation under neutral conditions with an extremely low overpotential value (~160 mV) and a high turnover frequency (TOF) number (~25 000 $\text{mmol}_{\text{O}_2} \text{ mol}^{-1}_{\text{Mn}} \text{ s}^{-1}$).^{7,13–16} Recently, X-ray analysis of the PSII structure at a resolution of 1.9 Å provided detailed structural information about the cubical Mn_4CaO_5 cluster stabilized by a surrounding peptide ligand.¹⁶ Four Mn atoms are oxo-bridged in asymmetric

positions and undergo successive changes in oxidation state, taking part in a so-called Kok cycle.^{12–18} It has also been suggested that O–O bond formation occurs at specific sites in the Mn_4CaO_5 cluster.¹⁶

The unique capabilities of the cubical Mn_4CaO_5 cluster have inspired the design of Mn-based catalysts for the OER.^{18–33} For example, the geometry of oxo-bridged Mn atoms has been synthetically controlled by designer organic ligands. $[\text{Mn}_4\text{O}_4\text{L}_6]^+$ ($\text{L} = (\text{MeOPh})_2\text{PO}_2$) or $[\text{Mn}_4\text{O}_4\text{L}_6]^-$ Nafion systems have been demonstrated as efficient water oxidation catalysts.³³ Recently, the Agapie group developed a $[\text{Mn}_3\text{CaO}_4]^{6+}$ core structure that was almost identical to that of the WOC in nature using trinucleating ligands.¹⁹ Moreover, using the $[\text{Mn}_3\text{CaO}_4]^{6+}$ core structure, they further synthesized $\text{Mn}_3\text{M}(\mu_4\text{-O})(\mu_2\text{-O})$ ($\text{M} = \text{Ca}^{2+}, \text{Sr}^{2+}, \text{Na}^+, \text{Zn}^{2+}$, and Y^{3+}) to

Received: March 15, 2014

Published: April 23, 2014



understand the role of redox-inactive metals in water oxidation catalysis.²⁰

As another route, various crystalline manganese oxide polymorphs and amorphous MnO_x have been investigated as water oxidation catalysts. Previous studies have reported that, among the various Mn oxide candidates, the materials whose structure and Mn valency were similar to those of the Mn_4CaO_5 cluster showed high activity. For example, the Dismukes group mimicked the $[\text{Mn}_4\text{O}_4]$ core units in the Mn_4CaO_5 cluster by removing the Li ions from LiMn_2O_4 Li ion battery cathode materials. Interestingly, the catalytically inactive LiMn_2O_4 materials converted into active $\lambda\text{-MnO}_2$, which has a $[\text{Mn}_4\text{O}_4]$ core unit. They assumed that the $[\text{Mn}_4\text{O}_4]$ core unit in the $\lambda\text{-MnO}_2$ was the origin of its high catalytic activity.³⁴ Recently, our group also found that a higher Mn(III) content in the OER catalysts can boost catalytic activity by increasing the degree of distortion in the Mn polyhedron.³⁵ Moreover, the Driess group developed amorphous MnO_x nanoparticles whose local structures and Mn atom valence states resembled those of the Mn_4CaO_5 cluster. They synthesized active, amorphous MnO_x ($1 < x < 2$) particles by oxidizing inactive, crystalline MnO nanoparticles using Ce^{IV} oxidants.³⁶ Moreover, the Dau group developed a new electrodeposition method to produce active MnO_x films that exhibited much higher activities than conventionally electrodeposited Mn oxide films. Using X-ray adsorption spectroscopy (XAS) analysis, they found that the newly developed electrodeposited amorphous MnO_x films had mixed valency (III/IV) and a disordered Mn geometry, which are recognized as important properties of the Mn_4CaO_5 cluster.³⁷ The Jaramillo group also found that active manganese oxide catalysts contained Mn(III) and Mn(IV) atoms, which are major components of the Mn_4CaO_5 cluster.³⁸

While Mn oxide compounds generally exhibit moderate catalytic abilities under basic conditions, their activity is significantly degraded at neutral pH.^{39,40} There have been several reports investigating the possible origin of the degradation mechanism of Mn oxide compounds under neutral pH. For example, the Nakamura group reported that the instability of the Mn(III) ions in the rigid and highly symmetric MnO_6 octahedron can decrease the activity of MnO_2 under neutral pH using electrochemical and spectroscopic analyses.²⁷ On the basis of theoretical approaches, they enhanced the catalytic ability by coordinating amide groups to the MnO_2 surface. They suggested that Mn–N bonds lower the symmetry of Mn octahedra and consequently Mn(III) can be stabilized in the octahedra under neutral pH.³¹ From the viewpoint of the degradation mechanism presented by the Nakamura group, the high catalytic activities of certain Mn oxide materials under neutral conditions might originate from their crystal structures, which can stabilize Mn(III) ions effectively. For example, the Dau group showed that distorted Mn polyhedra in amorphous MnO_x films can stabilize the Mn(III) ion and enhance OER catalysis. Moreover, the Dismukes group recently found that initially Mn(III) containing crystalline oxides displayed higher catalytic activities than Mn(IV)-based oxides.⁴¹ Therefore, it can be predicted that the catalysts that stabilize the Mn(III) state with ease during the OER at neutral pH may possess high activity under neutral conditions.

Herein, we synthesized a new water oxidation catalyst, $\text{Mn}_3(\text{PO}_4)_2\cdot3\text{H}_2\text{O}$, and identified its crystal structure and OER catalytic activity under neutral conditions. While transition metal phosphate compounds have been widely investigated as cathode materials for Li ion batteries, there has been no

attempt to study the OER catalytic performance of phosphate containing Mn-based crystals. We verified that the bulky phosphate polyhedron induces a less-ordered Mn geometry in $\text{Mn}_3(\text{PO}_4)_2\cdot3\text{H}_2\text{O}$, whose structure is similar to that of catalytic active Mn(III)-containing materials. Computational analysis revealed that distinctive structural features of $\text{Mn}_3(\text{PO}_4)_2\cdot3\text{H}_2\text{O}$ could successfully stabilize Mn(III) during water oxidation, leading to superior catalytic activity under neutral conditions.

■ EXPERIMENTAL SECTION

Manganese(II) phosphate hydrate was synthesized by adding 40 mL of 1.0 mM KH_2PO_4 in HEPES (1.85 mM, pH 7.4) to 40 mL of a 1.0 mM $\text{MnCl}_2\cdot4\text{H}_2\text{O}$ solution at 37 °C. The mixed solution slowly became turbid, indicating the formation of manganese(II) phosphate hydrate. After 3 h, the precipitate was centrifuged and washed three times with deionized (DI) water. The collected particles were then lyophilized before characterization. Inductively coupled plasma–mass spectrometry measurements and thermogravimetric analysis (TGA) revealed that the ratio of manganese atoms to phosphorus atoms in the manganese(II) phosphate hydrate crystal was 3:2 and that three water molecules were embedded per unit cell inside the crystal structure (Figure S1, Supporting Information). MnO , Mn_3O_4 , Mn_2O_3 , and MnO_2 nanoparticles were synthesized according to previous reports.

■ RESULTS

X-ray diffraction (XRD) analysis confirmed that the crystal structure of the synthesized manganese phosphate was $\text{Mn}_3(\text{PO}_4)_2\cdot3\text{H}_2\text{O}$. In this study, we discovered a new crystal, $\text{Mn}_3(\text{PO}_4)_2\cdot3\text{H}_2\text{O}$, whose crystal structure has never been identified completely. First, we attempted to match our diffraction pattern with the available crystal structures in the Inorganic Crystal Structure Database (ICSD), but the existing JCPDS data did not provide a match. Among the available data, the most similar pattern comes from JCPDS card no. 00-003-0426 (quality mark: low precision (O)) for poorly crystalline $\text{Mn}_3(\text{PO}_4)_2\cdot3\text{H}_2\text{O}$ (Figure S2 and Table S2, Supporting Information). However, no crystallographic information, such as the lattice parameter, atom coordination, Z factor, or plane index, is available. Therefore, we determined the accurate crystal structure of $\text{Mn}_3(\text{PO}_4)_2\cdot3\text{H}_2\text{O}$ by performing Rietveld refinement analysis and density functional theory (DFT) calculations, and we compared the simulated diffraction data with the experimental data (Figure 2d).

To computationally determine the crystal structure of $\text{Mn}_3(\text{PO}_4)_2\cdot3\text{H}_2\text{O}$, we focused on the crystal structure of switzerite ($\text{Mn}_3(\text{PO}_4)_2\cdot7\text{H}_2\text{O}$), which has been determined previously.⁴² Because the positions of the H atoms or the orientation of the water molecules were not well resolved in the experiment, we annealed the initial switzerite structure at 300 K for 3 ps using the first-principles molecular dynamics (MD) simulation (see computational details in the Supporting Information) and subsequently relaxed the structure at 0 K, obtaining the theoretical lattice parameters and atomic positions at equilibrium. According to the previous study, switzerite can convert to metaswitzerite ($\text{Mn}_3(\text{PO}_4)_2\cdot x\text{H}_2\text{O}$, $3 < x < 4$) by expelling water molecules and condensing the neutral layers along c in the framework structure.⁴² The transformation is topotactic; only a minor change in atomic position occurs during dehydration.⁴² Thus, in our first attempt to determine the structure, we assumed that the crystal structure of $\text{Mn}_3(\text{PO}_4)_2\cdot3\text{H}_2\text{O}$ could be derived in a topotactic manner by removing four water molecules from switzerite (Figure S3, Supporting Information). From the TGA analysis, we knew that there should be three water molecules per $\text{Mn}_3(\text{PO}_4)_2$.

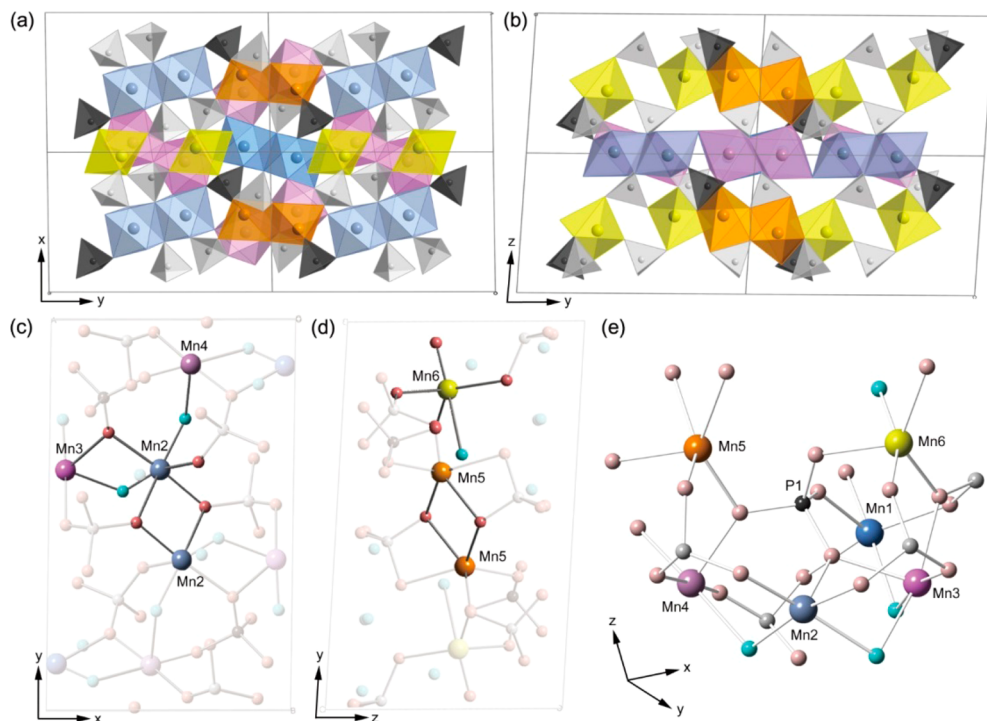


Figure 1. Schematic representation of crystalline $\text{Mn}_3(\text{PO}_4)_2 \cdot 3\text{H}_2\text{O}$. (a, b) Coordination and arrangement of each manganese atom. The larger spheres denote Mn atoms, and the smaller spheres denote phosphate molecules. The Mn(1), Mn(2), Mn(3), and Mn(4) atoms are illustrated in blue and purple. The Mn(5) and Mn(6) atoms are shown in orange and yellow, respectively. P(1) and P(2) display tetrahedral geometries, illustrated in black and gray, respectively. The octahedrons of Mn(1, 2, 3, and 4 positions) are connected, forming a $[\text{Mn}_4\text{O}_{10}(\text{H}_2\text{O})_4]_2$ sheet parallel to the (001) plane. (c) Mn(2) atoms are connected to each other by edge O–O sharing. The Mn(2) and Mn(3) atoms are bridged by edge O–O_w sharing, and the Mn(2) atoms are linked to Mn(4) atoms by O_w vertex sharing. (O_w: oxygen atom in a water molecule.) (d) Bonding character of Mn(5) and Mn(6). The Mn(5) atoms share two oxygen atoms with each other, forming Mn₂O₈ dimers. The Mn(6) atom does not share any atoms with other manganese atoms. (e) Spherical cluster around the P(1) site, with a radius of 4.5 Å, illustrating the asymmetrical arrangement of manganese atoms in the crystal.

Starting from the switzerite structure, we first removed three water molecules per formula unit in various combinations consistent with the structural information provided in ref 42. These structures were then fully relaxed using DFT methods, and the lowest-energy structure was chosen as the metaswitzerite. We then removed one additional water molecule per formula unit in every possible way and relaxed the structure again. The most stable structure was regarded as the theoretical structure of $\text{Mn}_3(\text{PO}_4)_2 \cdot 3\text{H}_2\text{O}$ and was triclinic, with $a = 8.640(3)$ Å, $b = 13.354(8)$ Å, $c = 8.455(1)$ Å, $\alpha = 86.50(1)^\circ$, $\beta = 105.12(5)^\circ$, $\gamma = 90.14^\circ$, and $Z = 4$.

All of the peaks obtained experimentally can be matched with those obtained from the simulated crystal structure. Close observation of the newly identified $\text{Mn}_3(\text{PO}_4)_2 \cdot 3\text{H}_2\text{O}$ crystals allowed us to distinguish six different manganese sites in one unit cell (Figure 1). As shown in Figure 1, the surrounding geometry of each manganese is symmetrically broken because $\text{Mn}_3(\text{PO}_4)_2 \cdot 3\text{H}_2\text{O}$ has triclinic crystal systems with the lowest symmetry. For example, Mn(1), Mn(2), Mn(3), and Mn(4) display distorted octahedral coordination, whereas Mn(5) and Mn(6) have a distorted trigonal bipyramidal (TBP) geometry (Figure 1). Water molecules are also positioned differently inside one unit cell ($[\text{Mn}_3(\text{PO}_4)_2 \cdot 3\text{H}_2\text{O}]_4$, $Z = 4$). Of the 12 water molecules in each unit cell, 8 water molecules (water 1) participate in bridging 2 manganese atoms in a Mn(1, 2, 3, and 4) sheet. Two water molecules (water 2) are bound to Mn(6). The other two water molecules (water 3) stay between two

sheets of Mn(1, 2, 3, and 4) without forming any coordinated bonds.

The asymmetric geometry of each manganese atom can be observed clearly by displaying the local structure around the P(1) position (Figure 1e). We measured the distances between manganese atoms in the simulated crystal structure. The shortest distance was 3.348 Å, between Mn(2) and Mn(3), and the longest was 6.408 Å, between Mn(3) and Mn(5), in the local structure around the P(1) position (Figure S4, Supporting Information). The average Mn–Mn distance was 3.411 Å, and the average Mn–O distance was 2.215 Å, which is much longer than the distances reported previously for Mn oxide based compounds⁴¹ (Figure S4 and Tables S2 and S3, Supporting Information). In PS II, the Mn₄CaO₅ cluster also has a distorted chair conformation and different distances between the four manganese atoms. In the cluster, the shortest distance is 2.8 Å, and the longest is 5.4 Å.¹⁶

The $\text{Mn}_3(\text{PO}_4)_2 \cdot 3\text{H}_2\text{O}$ crystals preferred to grow in sheetlike structures under our experimental conditions. When a fluorine-doped tin oxide (FTO) glass was dipped during the synthesis of $\text{Mn}_3(\text{PO}_4)_2 \cdot 3\text{H}_2\text{O}$, the sheets that could be found in bulk solution assembled into a flowerlike morphology, as shown in Figure 2a,b. High-resolution transmission electron microscopy (HRTEM) and selective area electron diffraction (SAED) analysis reveal that the two axes in the rectangular sheet were aligned in the [001] and [010] directions (Figure 2c).

In this study, to evaluate the catalytic activity of $\text{Mn}_3(\text{PO}_4)_2 \cdot 3\text{H}_2\text{O}$, well-known Mn oxide catalysts (MnO , Mn_3O_4 , Mn_2O_3 ,

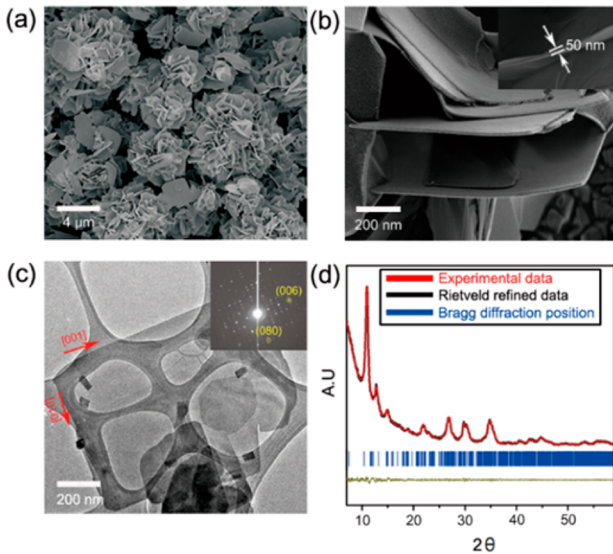


Figure 2. Characterization of $\text{Mn}_3(\text{PO}_4)_2 \cdot 3\text{H}_2\text{O}$. (a, b) SEM images of $\text{Mn}_3(\text{PO}_4)_2 \cdot 3\text{H}_2\text{O}$ crystals. (c) TEM image of a [001], [010]-oriented $\text{Mn}_3(\text{PO}_4)_2 \cdot 3\text{H}_2\text{O}$ sheet and SAED patterns (inset). (d) Rietveld-refined XRD patterns of $\text{Mn}_3(\text{PO}_4)_2 \cdot 3\text{H}_2\text{O}$ with experimental data (red dots) and calculated profiles (black line), resulting in a difference curve (yellow line) and Bragg diffraction positions (vertical bars). $R_{wp} = 1.05\%$, $R_p = 1.22\%$, $R_{exp} = 0.59\%$, and $\chi^2 = 1.79$.

and MnO_2) were synthesized for direct comparison. As an effort to minimize the effects of the crystal facet and size on the catalytic activity, we prepared Mn oxide compounds whose sizes were similar to that of $\text{Mn}_3(\text{PO}_4)_2 \cdot 3\text{H}_2\text{O}$. The synthetic procedure for each catalyst was referenced from the previous literature.⁴¹ XRD and scanning electron microscopy (SEM) analyses were conducted to identify the phase and morphology of each compound. XRD analysis clearly showed that all the synthesized Mn oxide nanoparticles had monophasic features without containing any secondary phase, and SEM analysis also revealed that the MnO and Mn_3O_4 nanoparticles had spherical-like shapes with diameters of 50–100 nm, while Mn_2O_3 and MnO_2 showed nanorod-like shapes with lengths of 80–300 nm (Figure S5, Supporting Information).

The water oxidation catalytic characteristics of the $\text{Mn}_3(\text{PO}_4)_2 \cdot 3\text{H}_2\text{O}$, MnO , Mn_3O_4 , Mn_2O_3 , and MnO_2 nanoparticles were evaluated by cyclic voltammetry (CV) in 0.5 M sodium phosphate electrolyte at pH 7. Each catalyst was deposited on the FTO substrate using a previously reported method.⁴³ The current values were normalized to the surface area of the catalyst on the working electrode. The surface area of the catalyst on the electrode was calculated by multiplying the weight of the catalyst on the electrode and the Brunauer–Emmett–Teller value of the catalyst. The OER activity curves were obtained by averaging the currents from the forward and reverse CV scans (for raw CV curves before polarization correction, see Figure S6, Supporting Information). The potentiostatic electrolysis of $\text{Mn}_3(\text{PO}_4)_2 \cdot 3\text{H}_2\text{O}$ yielded a current value similar to the average value (Figure 5 a, b). We expected that the average current was a reasonable approximation of the true steady-state current.⁴⁰ As shown in Figure 3a, the oxygen evolution ability of $\text{Mn}_3(\text{PO}_4)_2 \cdot 3\text{H}_2\text{O}$ was higher than that of the synthesized MnO , Mn_3O_4 , Mn_2O_3 , and MnO_2 nanoparticles. The current of $\text{Mn}_3(\text{PO}_4)_2 \cdot 3\text{H}_2\text{O}$ normalized to the surface area of the catalyst on the substrate was 0.316 mA/cm², whereas those of MnO , Mn_3O_4 , Mn_2O_3 , and MnO_2 were

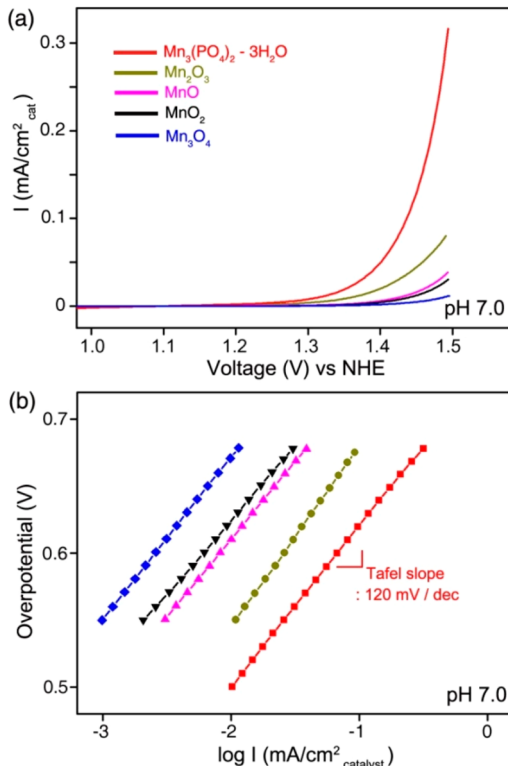


Figure 3. Electrochemical characterization of $\text{Mn}_3(\text{PO}_4)_2 \cdot 3\text{H}_2\text{O}$, MnO , Mn_3O_4 , Mn_2O_3 , and MnO_2 . (a) Polarization-corrected CV curves and (b) Tafel plots for $\text{Mn}_3(\text{PO}_4)_2 \cdot 3\text{H}_2\text{O}$, MnO , Mn_3O_4 , Mn_2O_3 , and MnO_2 spin-coated on the FTO substrate in which the current value was normalized to the surface area of the catalysts.

below 0.1 mA/cm² at the overpotential value of 680 mV (Figure 3a). Mn_2O_3 exhibited the highest catalytic activity (0.08 mA/cm²) among the four synthesized Mn oxide nanoparticles. Previously, the Dismukes group also observed that Mn_2O_3 exhibited the highest catalytic activity among the eight crystalline polymorphs of Mn oxides.⁴¹ The Tafel plot of each catalyst was obtained from the polarization-corrected CV curves. All Tafel slopes were approximately 120 mV/dec. The exchange current value of $\text{Mn}_3(\text{PO}_4)_2 \cdot 3\text{H}_2\text{O}$ was more than 3.5 times larger than that of MnO , Mn_3O_4 , Mn_2O_3 , and MnO_2 (Figure 3b).

The faradaic efficiency of $\text{Mn}_3(\text{PO}_4)_2 \cdot 3\text{H}_2\text{O}$ was measured by a fluorescence-based O_2 sensor. The catalyst was loaded onto the large FTO substrate (2.5 cm × 3 cm), and electrolysis was performed at the applied potential of 1.5 V versus NHE. Before electrolysis, the electrochemical cell was purged with high-purity Ar (99.999%) for 3 h, and the sensor was located in the headspace of the cell. The amount of evolved oxygen measured by the sensor is shown in Figure 4 (red line). A total of 34 μmol of oxygen molecules was evolved after 6000 s of electrolysis. When the electrolysis was terminated, there was a negligible increase in the oxygen molecules recorded by the sensor. The theoretical yield of oxygen during electrolysis was calculated from the total charge passed during the electrolysis (blue line). The faradaic efficiency of $\text{Mn}_3(\text{PO}_4)_2 \cdot 3\text{H}_2\text{O}$ was approximately 94%, indicating that the current measured by cyclic voltammetry primarily originated from the oxygen evolution reaction.

To characterize the stability of $\text{Mn}_3(\text{PO}_4)_2 \cdot 3\text{H}_2\text{O}$, we performed continuous potential cycling between 0.7 and 1.5

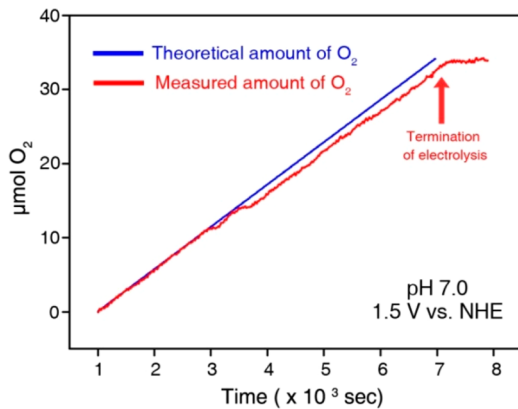


Figure 4. Amount of evolved O_2 molecules measured by fluorescence (blue line) and the theoretical amount of evolved O_2 (red line) during bulk electrolysis at the applied potential of 1.5 V vs NHE. The theoretical amount of O_2 molecules was calculated assuming a Faradaic efficiency of 100%.

V (vs NHE). As shown in Figure 5a, the CV currents of $Mn_3(PO_4)_2 \cdot 3H_2O$ remained nearly constant even after 100

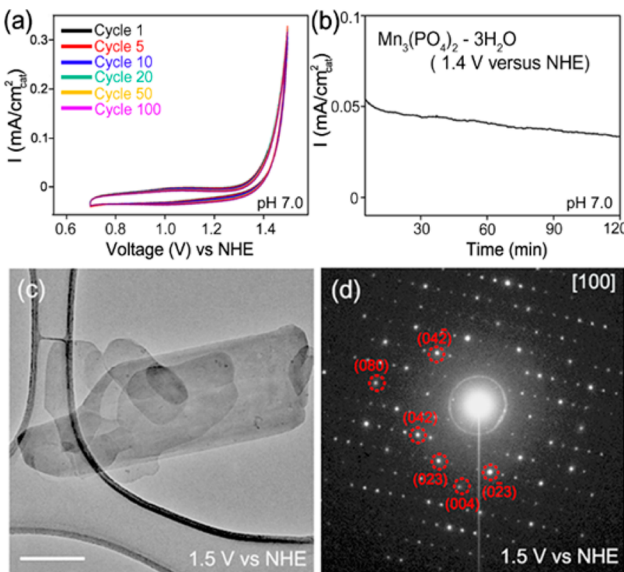


Figure 5. (a) CV curves of $Mn_3(PO_4)_2 \cdot 3H_2O$ showing the 1st, 5th, 10th, 20th, 50th, and 100th cycles. (b) Catalytic current profile obtained upon constant potential (1.4 V vs NHE) electrolysis under pH 7. As shown in the figure, considerable catalytic current was maintained after 2 h of electrolysis. (c) TEM and (d) SAED images of $Mn_3(PO_4)_2 \cdot 3H_2O$ after bulk electrolysis at 1.5 V for 3 h. The single-crystalline feature of $Mn_3(PO_4)_2 \cdot 3H_2O$ was maintained (scale bar: 200 nm). All the electrochemical reactions were performed in 0.5 M sodium phosphate buffer at pH 7.0.

cycles, indicating the high catalytic durability of $Mn_3(PO_4)_2 \cdot 3H_2O$. HRTEM analysis was performed to examine the phase stability of $Mn_3(PO_4)_2 \cdot 3H_2O$ under OER conditions. The single-crystalline feature of $Mn_3(PO_4)_2 \cdot 3H_2O$ was stably maintained after 30 min of bulk electrolysis at 1.5 V (Figure 5c, d). High phase stability of $Mn_3(PO_4)_2 \cdot 3H_2O$ was also confirmed by XRD measurement. It was revealed that there was no appreciable peak change or broadening after electrolysis. (Figure S7, Supporting Information)

We performed XAS and X-ray photoelectron spectroscopy (XPS) analysis to identify the detailed electronic structure of $Mn_3(PO_4)_2 \cdot 3H_2O$. XAS analysis provides detailed information on the oxidation state and coordination environments of metal ions. For instance, the Nocera group revealed the existence of mixed valency Co(III/IV) in amorphous cobalt oxide grains,⁴⁴ and the Jaramillo and the Dau groups also identified mixed valency in Mn(III/IV) in MnO_x films using X-ray absorption near edge structure (XANES) and XPS analyses.^{37,38}

In this study, we first examined the reference Mn oxide catalysts MnO , Mn_3O_4 , Mn_2O_3 , and MnO_2 , which are known to have Mn(II), Mn(II,III), Mn(III), and Mn(IV) average oxidation states, respectively. The Mn K-edge spectra for each catalyst at the catalytic resting state were recorded at room temperature, and the energy was calibrated using a glitch in the I_0 relative to the absorption edge of the Mn foil. As shown in Figure 6a, typical Mn pre-edge features were detected near 6540 eV in all Mn compounds, and a sequential shift in the XANES peak to higher energies was observed along with an increase in the Mn oxidation state. Interestingly, $Mn_3(PO_4)_2 \cdot 3H_2O$ had a slightly higher energy value than did MnO , which has the same Mn valency (Figure 6a, inset). It has been well documented that the ligand field strength has a direct effect on the energy position of the XANES spectrum;⁴⁵ thus, the positive energy shift of $Mn_3(PO_4)_2 \cdot 3H_2O$ might originate from the inductive effect of the phosphate anion. The strong P–O bond in the phosphate anion could induce the strong polarization of oxygen ions and lower the covalence of the metal–oxygen bond.⁴⁶ These inductive effects were observed by XPS analysis as well. We compared the binding energies of the Mn $2p_{1/2}$ peaks of $Mn_3(PO_4)_2 \cdot 3H_2O$ with those of the MnO particles. It was confirmed that the Mn $2p_{1/2}$ peak of $Mn_3(PO_4)_2 \cdot 3H_2O$ was positively shifted compared to the MnO particles, as expected from the XANES results. (Figure S8, Supporting Information) In addition, we investigated the XPS peak difference between the as-prepared $Mn_3(PO_4)_2 \cdot 3H_2O$ (before the OER) and the bulk-electrolyzed $Mn_3(PO_4)_2 \cdot 3H_2O$ (after the OER). Even after 1 h of bulk electrolysis, the peak position of Mn $2p_{1/2}$ remained unchanged compared with that of the as-prepared samples (Figure 6c). Because the XPS measurement is surface-sensitive,³⁵ the invariance of the XPS Mn peak shows that the oxidation states of Mn both in the bulk and at the surface were maintained.

Furthermore, we performed in situ XANES analysis to clearly observe the possible change of the Mn oxidation state during the OER. The electrochemical cell for in situ XANES analysis was designed as shown in Figure S9 (Supporting Information). The solution resistance of the cell was $\sim 42 \Omega$, and the catalytic current exhibited similar values as those in Figure 3a. Before electrolysis, the Mn K-edge spectra of $Mn_3(PO_4)_2 \cdot 3H_2O$ in 0.5 M sodium phosphate buffer was compared with that of powder $Mn_3(PO_4)_2 \cdot 3H_2O$. There was a negligible difference between the two spectra, indicating that $Mn_3(PO_4)_2 \cdot 3H_2O$ did not undergo oxidation in the aqueous conditions. After measuring the Mn K-edge spectra of $Mn_3(PO_4)_2 \cdot 3H_2O$ before electrolysis, $Mn_3(PO_4)_2 \cdot 3H_2O$ was electrolyzed at the applied potential of 1.5 V vs NHE for 3 h. The in situ XANES spectra corresponding to the Mn K-edge spectra of $Mn_3(PO_4)_2 \cdot 3H_2O$ were monitored during the electrolysis. As shown in Figure 6b, the spectra of $Mn_3(PO_4)_2 \cdot 3H_2O$ were maintained during electrolysis process. In addition, even after we spanned the 6540–6550 eV region, there was no peak shift before and after electrolysis, indicating the invariance of valency of Mn

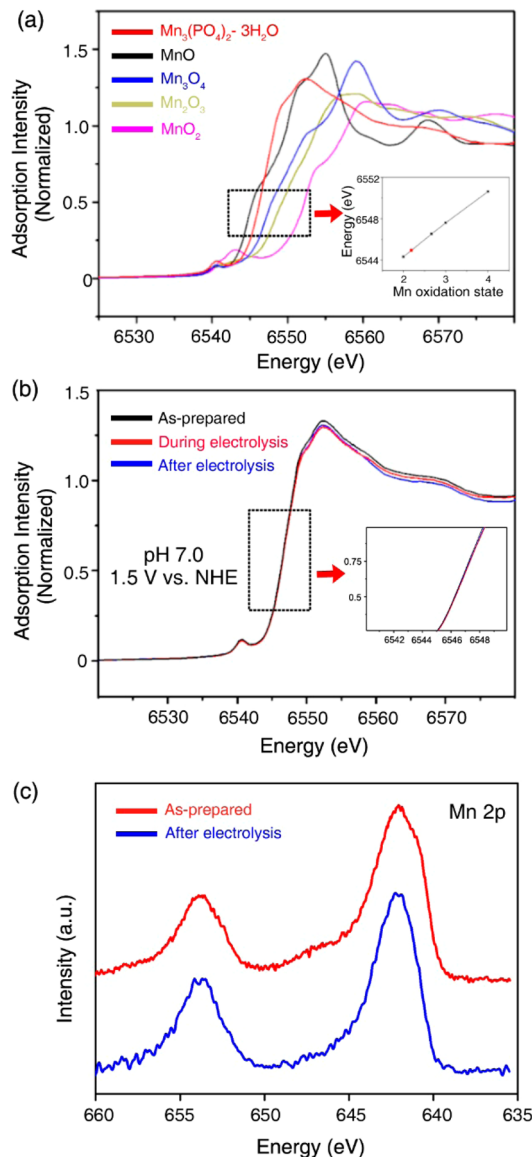


Figure 6. (a) Ex situ XANES Mn K-edge spectra of $\text{Mn}_3(\text{PO}_4)_2 \cdot 3\text{H}_2\text{O}$, MnO , Mn_3O_4 , Mn_2O_3 , and MnO_2 powders. The inset shows the oxidation state of the Mn atoms in $\text{Mn}_3(\text{PO}_4)_2 \cdot 3\text{H}_2\text{O}$. On the basis of the spectra of Mn based oxide materials, $\text{Mn}_3(\text{PO}_4)_2 \cdot 3\text{H}_2\text{O}$ showed a value slightly higher than 2+. (b) In situ XANES spectra corresponding to the Mn K-edge of $\text{Mn}_3(\text{PO}_4)_2 \cdot 3\text{H}_2\text{O}$ before, during, and after bulk-electrolysis at an applied potential of 1.5 V vs NHE for 3 h. The inset displays the enlarged XANES edge region. (c) XPS spectra of the Mn 2p region of the as-prepared and bulk-electrolyzed $\text{Mn}_3(\text{PO}_4)_2 \cdot 3\text{H}_2\text{O}$ at an applied potential of 1.5 V vs NHE for 3 h. All the electrochemical reactions were performed in 0.5 M sodium phosphate buffer at pH 7.0.

atoms during the water oxidation catalysis (Figure 6b inset). Although the fluorescence yield mode that was used to obtain the Mn K-edge spectra in this study is bulk-sensitive, our results indicate that the oxidation state of Mn did not significantly change during the OER. If $\text{Mn}_3(\text{PO}_4)_2 \cdot 3\text{H}_2\text{O}$ underwent phase transformation to Mn (III) or Mn (IV) containing materials, the Mn K-edge spectra of the electrolyzed $\text{Mn}_3(\text{PO}_4)_2 \cdot 3\text{H}_2\text{O}$ during the OER would have shifted toward the higher energy region compared with that of as-prepared $\text{Mn}_3(\text{PO}_4)_2 \cdot 3\text{H}_2\text{O}$.

■ DISCUSSION

To theoretically investigate the enhanced catalytic ability of $\text{Mn}_3(\text{PO}_4)_2 \cdot 3\text{H}_2\text{O}$, we first focused on the crystal structure of $\text{Mn}_3(\text{PO}_4)_2 \cdot 3\text{H}_2\text{O}$. Indeed, the crystal structure has been regarded as one of the major sources of catalytic ability. Especially for Mn-containing catalysts, the stabilization of Mn(III) during the OER and the initial content of Mn(III) in the crystal structure are important, as evident in the WOC in PSII and in Mn_2O_3 . Recent reports revealed that the transition from Mn(II) to Mn(III) could be a rate-limiting step in the OER catalysis of Mn-based oxide catalysts.²⁷ In this regard, we performed a computation to observe the effect on crystal structure when Mn(II) ions inside the catalyst were oxidized to Mn(III). First, to understand the effect of crystal structure on the stabilization of Mn(III), we selected β - MnO_2 , which has been mainly investigated for correlating structure and oxidation state. According to a recently proposed mechanism,²⁷ the surface oxidation state of β - MnO_2 is spontaneously reduced to Mn(II) by electron injection from H_2O and then electro-oxidized into Mn(III) when an electric potential of ~1.5 V with respect to NHE is applied. Thus, we first negatively charged β - MnO_2 by adding a number of electrons to enforce the Mn(II) state in β - MnO_2 ($\text{Mn}(\text{IV}) \rightarrow \text{Mn}(\text{II})$) and then oxidized this negatively charged β - MnO_2 to form Mn(III) ($\text{Mn}(\text{II}) \rightarrow \text{Mn}(\text{III})$). The pair distribution function showed that the average distance of Mn–O was 1.916 Å, which split into 1.840 and 1.916 Å as a result of the oxidation of Mn(II) to Mn(III) (Figure 7a). This small splitting indicates that the Jahn–Teller (J–T) distortion is significantly hindered. Then, we positively charged $\text{Mn}_3(\text{PO}_4)_2 \cdot 3\text{H}_2\text{O}$ by reducing a number of electrons, such that all the Mn atoms were converted from Mn(II) to Mn(III). The resulting pair distribution function of Mn–O in Figure 7b demonstrates that the Mn–O bond lengths are split into various values of 1.980–2.524 Å upon full oxidation, clearly demonstrating significant J–T distortion in the Mn(III) octahedra of up to 0.5 Å. We also performed similar calculations for MnO , which has the same resting Mn valency (Figure 7c). The Mn(II)–O bond length (2.240 Å on average) split into 2.090 and 2.440 Å in the Mn(III) configuration, indicating a degree of J–T distortion similar to that observed for $\text{Mn}_3(\text{PO}_4)_2 \cdot 3\text{H}_2\text{O}$.

As another standard to gauge the stability of Mn(III), we examined the average pressure when all the Mn atoms were in the Mn(III) configuration (Figure 7d). A large pressure implies a tendency for the lattice to be distorted and destabilized when Mn(III) atoms are abundant. As shown in Figure 7d, the magnitude of pressure follows the order $\text{MnO}_2 > \text{MnO} > \text{Mn}_3(\text{PO}_4)_2 \cdot 3\text{H}_2\text{O}$. Interestingly, the catalytic activity in Figure 3a exactly follows the reverse order. Therefore, in combination with the above analysis of the J–T distortion, we conclude that the structural flexibility that stabilizes the Mn(III) state could explain the high catalytic activity of $\text{Mn}_3(\text{PO}_4)_2 \cdot 3\text{H}_2\text{O}$.

Because the catalytic reaction occurs at the surface, it would be worthwhile to study the surface.³⁵ It was found in Figure 2c that mainly (100) surfaces are exposed, and it is believed that this surface direction mainly contributes to the catalytic effect. We modeled the (100) surface by considering a stoichiometric slab with a thickness of ~16 Å, as shown in Figure 8. Of the two types of stoichiometric (100) surfaces, the more stable one was investigated. The atoms in the shaded area are fixed to bulk positions to emulate the semi-infinite surface model. One monolayer of water molecules was introduced on the

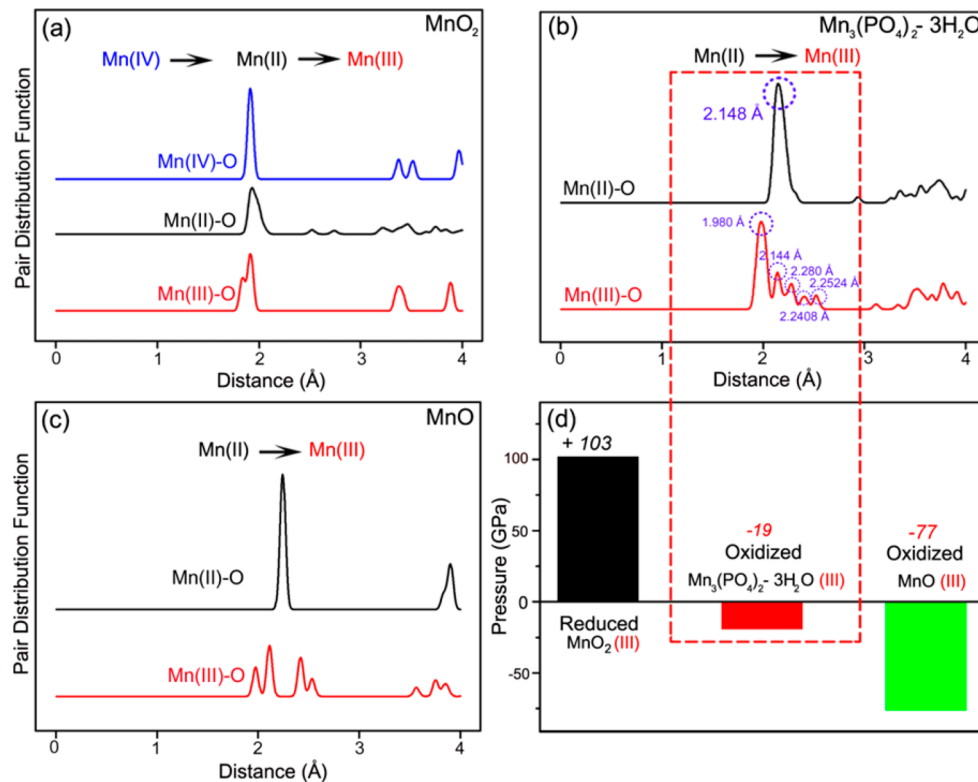


Figure 7. Pair distribution functions of manganese atoms (a) in pristine MnO₂ (blue) and in reduced manganese oxide as Mn(II) (black) and Mn(III) (red); (b) in pristine Mn₃(PO₄)₂·3H₂O (black) and in oxidized manganese phosphate (red), in which all Mn(II) atoms were intentionally oxidized to Mn(III); and (c) in pristine MnO (black) and in oxidized manganese oxide (red). The pair distribution function near 2 Å in Mn₃(PO₄)₂·3H₂O indicates that the Mn–O bonds originated from phosphate groups. In contrast to MnO₂, the split of the pair distribution function from black to red in Mn₃(PO₄)₂·3H₂O and in MnO indicates J–T distortion. (d) The pressure on the cell of each Mn compound when Mn was reduced or oxidized to the 3+ state. It is noted that the pressure is unrealistically large because all the Mn atoms change the charge state.

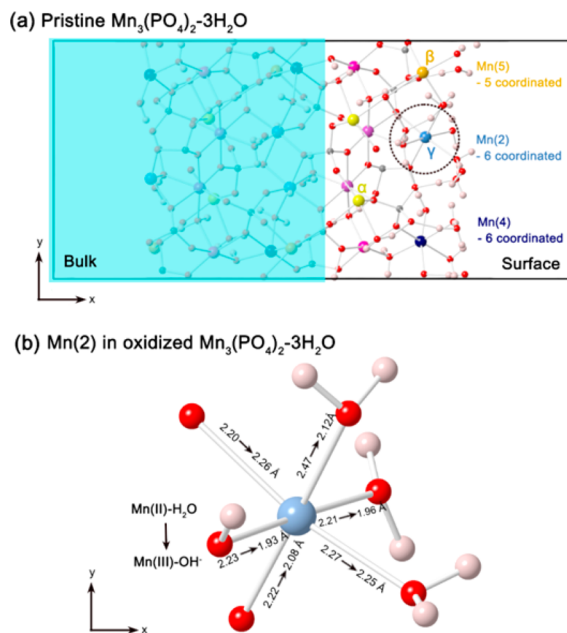


Figure 8. Surface structure of Mn₃(PO₄)₂·3H₂O. (a) (100) surface stabilized with water molecules; the atoms in the shaded area are fixed to bulk positions. (b) Bonding geometry of the J–T distorted surface Mn(2) atom of oxidized manganese phosphate, in which some Mn(II) atoms were intentionally oxidized to Mn (III).

catalytically active surface to consider the water environment, and the structure was optimized through a molecular dynamics simulation at 300 K.

In the bulk-terminated surface, the exposed Mn(2), Mn(4), and Mn(5) atoms are coordinately unsaturated but are stabilized with water molecules, and consequently, their bulk coordination numbers (6-, 6-, and 5-fold) are maintained. To compare the activities of each surface Mn ion, we took electrons away from the system one by one and relaxed the structures. Interestingly, the oxidation of Mn(II) to Mn(III) occurred first at the 5-fold Mn(6), marked as α . It is shown that the 5-fold Mn(6) at the subsurface near the PO₄ dangling bond (α), the 5-fold Mn(5) at surface (β), and the 6-fold Mn(2) close to the PO₄ dangling bond (γ) were oxidized to Mn(III) sequentially, indicating that the 5-fold Mn atoms are catalytically more active than the 6-fold Mn atoms. Although this Mn(6) is at the subsurface, coordinated water molecules have an open channel to the surface of which the width is \sim 3.4 Å; thus, the coordinated water on Mn(6) is an active water that can interact with environment during catalysis (Figure S10, Supporting Information). In this regard, the structure of subsurface do not have to be reconstructed during the water oxidation catalysis, and consequently, the crystallinity of the Mn₃(PO₄)₂·3H₂O can be maintained at the surface. We believe that 5-fold subsurface Mn(6) can be the active site for water oxidation. Interestingly, it can also be observed in Figure 8b that the 6-fold Mn(2) atom on the surface undergoes J–T distortion, as in the bulk. Furthermore, owing to the PO₄ dangling bonds near the Mn atoms, some Mn(II)–H₂O bonds

on the surface and subsurface are found to transfer hydrogens to the dangling bonds, producing Mn(III) --OH^- . This suggests that the PO_4 dangling bonds in the surface region act as proton acceptors that facilitate the oxidation of the Mn atoms. Specifically, in the surface model that we suggested in Figure 8a, there is a PO_4 dangling bond near the channel connecting subsurface Mn(6) to the surface where the dangling bond can mediate the proton-coupled electron transfer (PCET) between the active water and the environment. Actually, the phosphate group can participate in PCET as proton acceptors during OER catalysis. Indeed, it was found that electrodeposited Co–Pi films follow PCET reaction during water oxidation by transferring protons to the phosphate anion in the electrolyte.⁹ Although more experimental evidence is required to determine whether our catalyst follows PCET reaction during the OER catalysis, we thought that the phosphate ions can facilitate the oxidation of the Mn– OH_2 centers by PCET reaction based on our computational results. Therefore, in addition to the structural flexibility facilitating the J–T distortion and the 5-fold Mn(II) atoms that are more conducive to oxidation than the 6-fold Mn(II), the surface catalytic effect increases owing to the PO_4 dangling bonds near the Mn atoms.

In conclusion, we presented a new crystalline phase, $\text{Mn}_3(\text{PO}_4)_2 \cdot 3\text{H}_2\text{O}$, that is generated by an environmentally benign process and acts as an efficient OER catalyst. On the basis of XRD analysis and DFT calculations, we found that Mn atoms have an asymmetric geometry in the crystal and display a distorted crystal field with phosphate groups and water molecules. $\text{Mn}_3(\text{PO}_4)_2 \cdot 3\text{H}_2\text{O}$ exhibits superior catalytic performance at neutral pH. DFT theoretical calculations verified the experimental observation that Mn(II) atoms can be easily oxidized into Mn(III) intermediate species through J–T distortion, which is stabilized by its structural nature, the distorted and flexible crystal field around the Mn atoms, and the water molecules inside the crystal. We expect that the discovery of this new $\text{Mn}_3(\text{PO}_4)_2 \cdot 3\text{H}_2\text{O}$ crystal and the relationship between its structural features and catalytic performance will provide insights useful for the development of divalent Mn-based catalysts.

ASSOCIATED CONTENT

Supporting Information

Full experimental materials and methods; tables of crystal structures of manganese based oxide and phosphate compounds, bond lengths, and Mn–Mn distances; and figures showing TGA, XRD pattern comparisons, crystal structures, distance between different Mn sites, characterization of synthesized nanoparticles, CV curves, XRD analysis, XPS spectra, designed electrochemical cell for in situ XANES analysis, and surface structure. This material is available free of charge via the Internet at <http://pubs.acs.org>.

AUTHOR INFORMATION

Corresponding Author

nkita@snu.ac.kr

Author Contributions

[†]These authors contributed equally.

Notes

The authors declare no competing financial interests.

ACKNOWLEDGMENTS

This research was supported by the Basic Science Research Program through the National Research Foundation of Korea (NRF) funded by the Ministry of Science, ICT & Future (grant no. 2011-0011225) and the Global Frontier R&D Program on Center for Multiscale Energy System funded by the National Research Foundation under the Ministry of Science, ICT & Future, Korea. (0420-20130104).

REFERENCES

- Lewis, N. S.; Nocera, D. G. *Proc. Natl. Acad. Sci. U.S.A.* **2006**, *103*, 15729.
- Bard, A. J.; Fox, M. A. *Acc. Chem. Res.* **1995**, *28*, 141.
- Gust, D.; Moore, T. A.; Moore, A. L. *Acc. Chem. Res.* **2009**, *42*, 1890.
- Swierk, J. R.; Mallouk, T. E. *Chem. Soc. Rev.* **2013**, *42*, 2357.
- Grätzel, M. *Nature* **2001**, *414*, 338.
- Meyer, T. J. *Acc. Chem. Res.* **1989**, *22*, 163.
- Barber, J. *Chem. Soc. Rev.* **2009**, *38*, 185.
- Youngblood, W. J.; Lee, S.-H. A.; Kobayashi, Y.; Hernandez-Pagan, E. A.; Hoertz, P. G.; Moore, T. A.; Moore, A. L.; Gust, D.; Mallouk, T. E. *J. Am. Chem. Soc.* **2009**, *131*, 926.
- Kanan, M. W.; Nocera, D. G. *Science* **2008**, *321*, 1072.
- Duan, L.; Bozoglian, F.; Mandal, S.; Stewart, B.; Privalov, T.; Llobet, A.; Sun, L. *Nat. Chem.* **2012**, *4*, 418.
- Zhao, Y.; Swierk, J. R.; Megiatto, J. D.; Sherman, B.; Youngblood, W. J.; Qin, D.; Lentz, D. M.; Moore, A. L.; Moore, T. A.; Gust, D.; Mallouk, T. E. *Proc. Natl. Acad. Sci. U.S.A.* **2012**, *109*, 15612.
- Betley, T. A.; Wu, Q.; Van Voorhis, T.; Nocera, D. G. *Inorg. Chem.* **2008**, *47*, 1849.
- Loll, B.; Kern, J.; Saenger, W.; Zouni, A.; Biesiadka, J. *Nature* **2005**, *438*, 1040.
- Yano, J.; Kern, J.; Sauer, K.; Latimer, M. J.; Pushkar, Y.; Biesiadka, J.; Loll, B.; Saenger, W.; Messinger, J.; Zouni, A.; Yachandra, V. K. *Science* **2006**, *314*, 821.
- Ferreira, K. N.; Iverson, T. M.; Maghlaoui, K.; Barber, J.; Iwata, S. *Science* **2004**, *303*, 1831.
- Umena, Y.; Kawakami, K.; Shen, J.-R.; Kamiya, N. *Nature* **2011**, *473*, 55.
- Roelofs, T. A.; Liang, W.; Latimer, M. J.; Cinco, R. M.; Rompel, A.; Andrews, J. C.; Sauer, K.; Yachandra, V. K.; Klein, M. P. *Proc. Natl. Acad. Sci. U.S.A.* **1996**, *93*, 3335.
- Dau, H.; Iuzzolino, L.; Dittmer, J. *Biochim. Biophys. Acta, Bioenerg.* **2001**, *1503*, 24.
- Kanady, J. S.; Tsui, E. Y.; Day, M. W.; Agapie, T. *Science* **2011**, *333*, 733.
- Tsui, E. Y.; Tran, R.; Yano, J.; Agapie, T. *Nat. Chem.* **2013**, *5*, 293.
- Ruettinger, W. F.; Ho, D. M.; Dismukes, G. C. *Inorg. Chem.* **1999**, *38*, 1036.
- Hocking, R. K.; Brimblecombe, R.; Chang, L.-Y.; Singh, A.; Cheah, M. H.; Glover, C.; Casey, W. H.; Spiccia, L. *Nat. Chem.* **2011**, *3*, 461.
- McCool, N. S.; Robinson, D. M.; Sheats, J. E.; Dismukes, G. C. *J. Am. Chem. Soc.* **2011**, *133*, 11446.
- Hu, X. L.; Piccinin, S.; Laio, A.; Fabris, S. *ACS Nano* **2012**, *6*, 10497.
- Kanan, M. W.; Yano, J.; Surendranath, Y.; Dincă, M.; Yachandra, V. K.; Nocera, D. G. *J. Am. Chem. Soc.* **2010**, *132*, 13692.
- Najafpour, M. M.; Ehrenberg, T.; Wiechen, M.; Kurz, P. *Angew. Chem., Int. Ed.* **2010**, *49*, 2233.
- Takashima, T.; Hashimoto, K.; Nakamura, R. *J. Am. Chem. Soc.* **2011**, *134*, 1519.
- Mohammad, A. M.; Awad, M. I.; El-Deab, M. S.; Okajima, T.; Ohnsaka, T. *Electrochim. Acta* **2008**, *53*, 4351.
- Morita, M.; Iwakura, C.; Tamura, H. *Electrochim. Acta* **1977**, *22*, 325.

- (30) Morita, M.; Iwakura, C.; Tamura, H. *Electrochim. Acta* **1979**, *24*, 357.
- (31) Takashima, T.; Hashimoto, K.; Nakamura, R. *J. Am. Chem. Soc.* **2012**, *134*, 18153.
- (32) Morita, M.; Iwakura, C.; Tamura, H. *Electrochim. Acta* **1978**, *23*, 331.
- (33) Brimblecombe, R.; Koo, A.; Dismukes, G. C.; Swiegers, G. F.; Spiccia, L. *J. Am. Chem. Soc.* **2010**, *132*, 2892.
- (34) Robinson, D. M.; Go, Y. B.; Greenblatt, M.; Dismukes, G. C. *J. Am. Chem. Soc.* **2010**, *132*, 11467.
- (35) Park, J.; Kim, H.; Jin, K.; Lee, B. J.; Park, Y.-S.; Kim, H.; Park, I.; Yang, K. D.; Jeong, H.-Y.; Kim, J.; Hong, K. T.; Jang, H. W.; Kang, K.; Nam, K. T. *J. Am. Chem. Soc.* **2014**, *136*, 4201.
- (36) Indra, A.; Menezes, P. W.; Zaharieva, I.; Baktash, E.; Pfommer, J.; Schwarze, M.; Dau, H.; Driess, M. *Angew. Chem., Int. Ed.* **2013**, *52*, 13206.
- (37) Zaharieva, I.; Najafpour, M. M.; Wiechen, M.; Haumann, M.; Kurz, P.; Dau, H. *Energy Environ. Sci.* **2011**, *4*, 2400.
- (38) Gorlin, Y.; Lassalle-Kaiser, B.; Benck, J. D.; Gul, S.; Webb, S. M.; Yachandra, V. K.; Yano, J.; Jaramillo, T. F. *J. Am. Chem. Soc.* **2013**, *135*, 8525.
- (39) Magnuson, A.; Frapart, Y.; Abrahamsson, M.; Horner, O.; Åkermark, B.; Sun, L.; Girerd, J.-J.; Hammarström, L.; Styring, S. *J. Am. Chem. Soc.* **1998**, *121*, 89.
- (40) Lee, S. W.; Carlton, C.; Risch, M.; Surendranath, Y.; Chen, S.; Furutsuki, S.; Yamada, A.; Nocera, D. G.; Shao-Horn, Y. *J. Am. Chem. Soc.* **2012**, *134*, 16959.
- (41) Robinson, D. M.; Go, Y. B.; Mui, M.; Gardner, G.; Zhang, Z.; Mastrogiovanni, D.; Garfunkel, E.; Li, J.; Greenblatt, M.; Dismukes, G. C. *J. Am. Chem. Soc.* **2013**, *135*, 3494.
- (42) Zanazzi, P. F.; Leavens, P. B.; White, J. S. *Am. Mineral.* **1986**, *71*, 1224.
- (43) Gardner, G. P.; Go, Y. B.; Robinson, D. M.; Smith, P. F.; Hadermann, J.; Abakumov, A.; Greenblatt, M.; Dismukes, G. C. *Angew. Chem., Int. Ed.* **2012**, *51*, 1616.
- (44) Kanan, M. W.; Yano, J.; Surendranath, Y.; Dincă, M.; Yachandra, V. K.; Nocera, D. G. *J. Am. Chem. Soc.* **2010**, *132*, 13692.
- (45) Sarangi, R. *Coord. Chem. Rev.* **2013**, *257*, 459.
- (46) Padhi, A. K.; Nanjundaswamy, K. S.; Goodenough, J. B. *J. Electrochem. Soc.* **1997**, *144*, 1188.